Distinct Nucleation and Growth Kinetics of Amorphous SrTiO<sub>3</sub> on (001) SrTiO<sub>3</sub> and SiO<sub>2</sub>/Si: A Step towards New Architectures

Yajin Chen<sup>1†</sup>, M. Humed Yusuf<sup>1†</sup>, Yingxin Guan<sup>1</sup>, RB Jacobson<sup>1</sup>, Max G. Lagally<sup>1</sup>, Susan E.

Babcock<sup>1</sup>, Thomas F. Kuech<sup>2</sup> and Paul G. Evans<sup>1\*</sup>

<sup>1</sup> Department of Materials Science & Engineering, University of Wisconsin-Madison, Madison, WI 53706

<sup>2</sup> Department of Chemical & Biological Engineering, University of Wisconsin-Madison,
Madison, WI 53706

†These authors contributed equally to this work.

KEYWORDS: sputter deposition, SrTiO<sub>3</sub>, epitaxy, crystallization, nucleation, 3D structures

ABSTRACT: The integration of emerging complex-oxide compounds into sophisticated nanoscale single-crystal geometries faces significant challenges arising from the kinetics of vaporphase thin-film epitaxial growth. A comparison of the crystallization of the model perovskite SrTiO<sub>3</sub> (STO) on (001) STO and oxidized (001) Si substrates indicates that there is a viable alternative route that can yield three-dimensional epitaxial synthesis, an approach in which STO is crystallized from an amorphous thin film by post-deposition annealing. The crystallization of amorphous STO on single-crystal (001) STO substrates occurs via solid-phase epitaxy (SPE), without nucleation and with a temperature-dependent amorphous/crystalline interface velocity. In comparison, the crystallization of STO on SiO<sub>2</sub>/(001) Si substrates requires nucleation, resulting in a polycrystalline film with crystal sizes on the order of 10 nm. A comparison of the temperature dependence of the nucleation and growth processes for these two substrates indicates that it will be possible to create crystalline STO materials using low-temperature crystallization from a crystalline seed, even in the presence of interfaces with other materials. These processes provide a potential route for the formation of single crystals with intricate three-dimensional nanoscale geometries.

## Introduction

The integration of complex-oxide crystals in three-dimensional nanoscale geometries has the potential to enable a variety of new materials, including those exhibiting facile oxygen transport, single-crystal composites for the control of thermal properties, and large volumes of nanostructures in which mechanical, optical, and electronic phenomena are modified by size effects. Considerable effort has been devoted to the synthesis of crystalline complex oxides in the form of thin films yielding low defect densities, while simultaneously controlling the phase, strain, crystallographic orientation, and elemental composition. This creation of single-crystalline oxide layers via heteroepitaxy largely employs growth from a vapor, relying on elevated surface temperatures to favor processes facilitating long-range surface diffusion and the formation of the crystalline phase directly at the surface. Deposition in line-of-sight geometries in epitaxial deposition via molecular beam epitaxy, sputter ion deposition, or pulsed-laser deposition most often produces two-dimensional thin-film heterostructures. Complementary growth techniques facing different kinetic constraints have the potential to allow deposition and crystallization under much more flexible conditions.

The two-dimensional constraint facing heteroepitaxy from the vapor can in principle be lifted by crystallizing the desired complex oxide crystalline phase from an initially amorphous form, which can be deposited using techniques that do not rely on maintaining line-of-sight during deposition. This approach can be applied to complex geometries by crystallizing layers on a patterned three-dimensional substrate, part of which is composed of crystalline seeds.<sup>7-8</sup> The eventual use of crystallization to create complex geometries requires understanding the propagation of a crystal growth front from a crystalline seed and nucleation either within the amorphous material or at interfaces that do not act as crystalline seeds.

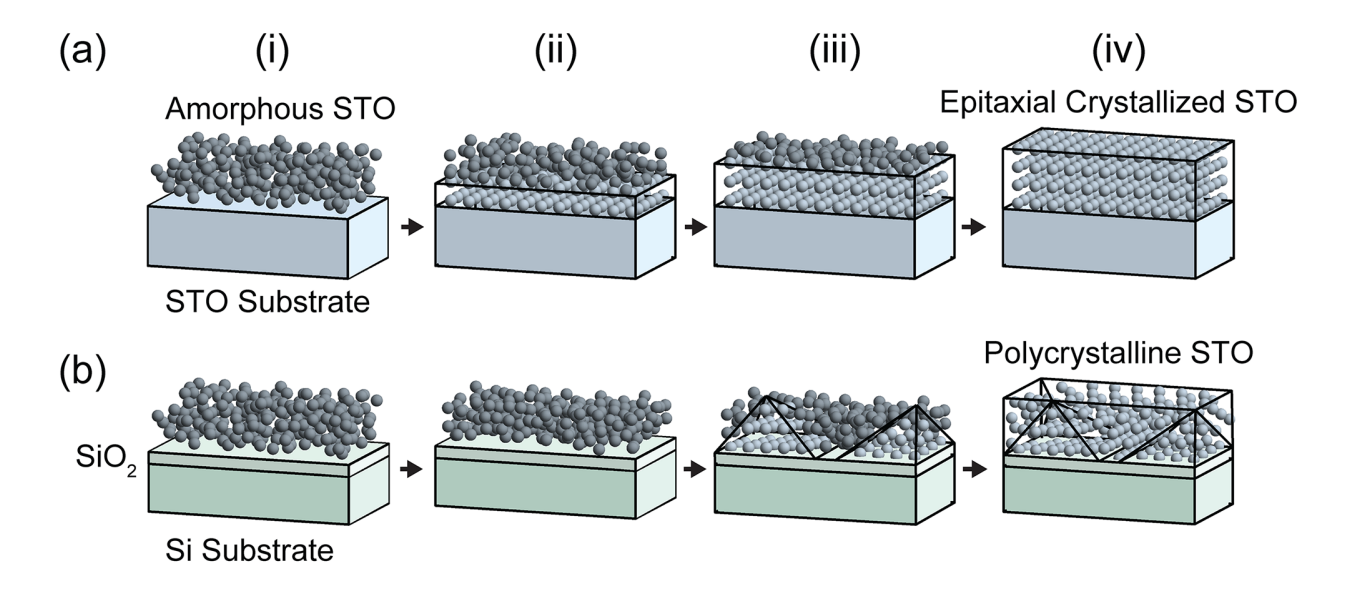


Figure 1. (a) Schematic of the crystallization of amorphous STO on (001) STO substrates by SPE: (i) As-deposited amorphous STO layer, (ii) and (ii) Crystallization of STO through the motion of the amorphous/crystalline interface towards the surface, and (iv) Fully crystallized epitaxial STO thin film. (b) Schematic of the crystallization of amorphous STO on SiO<sub>2</sub>/(001) Si substrates by nucleation and growth: (i) As-deposited amorphous STO, (ii) Persistence of the amorphous structure in the interval before nucleation, (iii) Polycrystalline nucleation and growth of STO crystals, and (iv) Fully crystallized polycrystalline STO thin film.

Here we report the relative rates of nucleation and growth in the crystallization of the model complex oxide SrTiO<sub>3</sub> (STO) on surfaces differing in structure and composition and demonstrate that the scaling of these rates is favorable for crystallization in complex geometries. The crucial insight is that there is a difference in the kinetics of crystallization of amorphous STO thin films deposited on two substrates: (i) (001) STO single-crystals and (ii) Si surfaces with a native oxide, termed SiO<sub>2</sub>/(001) Si. The amorphous-to-crystalline transformation is dramatically different on the two substrates, as shown schematically in Fig. 1. We show here that the temperature dependence

of nucleation and growth processes for STO crystals reveals that the effective activation energy for nucleation of crystalline STO from an amorphous STO layer is higher than the activation energy of the motion of the crystal/amorphous interface. It thus is particularly important to consider crystallization at low temperatures, approximately 450 °C in the present study, where the rates of crystal growth for STO on STO and nucleation for STO on SiO<sub>2</sub>/Si are significantly different and favor the growth of large STO crystals even in the presence of interfaces with other materials.

STO serves as a model for perovskite systems of technological interest and has experimental advantages arising from its simple-cubic symmetry and lack of competing polymorphic phases. Because of the similarity of structural and chemical issues, it is likely that the growth kinetics of STO are applicable to the formation of structurally similar complex oxides on other crystalline substrates and in various geometries. In addition, STO itself has a range of functionalities, including as a high-k gate insulator in field effect transistors, a nanoscale ferroelectric, and through formation of two-dimensional electron gases at LaAlO<sub>3</sub>/SrTiO<sub>3</sub> (LAO/STO) interfaces. The crystallization of STO on single-crystal (001) STO substrates occurs through solid-phase epitaxy (SPE), the motion of a smooth amorphous/crystalline interface towards the surface. The kinetics of SPE in STO have been probed in amorphous layers created by ion implantation, sputter deposition, and pulsed-laser deposition, revealing that interface velocities are thermally

In contrast to SPE, much less is known about crystal nucleation in amorphous complex oxide thin films on substrates, such as amorphous SiO<sub>2</sub>/(001) Si, which do not provide a crystalline

activated and that a planar interface is preserved. The series of kinetic processes is more complex

at high temperatures, where motion of the interface by SPE is accompanied by nucleation of

crystals in the region of the film far from the amorphous/crystalline interface.<sup>14</sup>

template for epitaxial STO. Molecular dynamics simulations of other oxide materials show that nucleation involves a set of atomic-scale processes associated with the rearrangement of the nanometer scale structure into local metal-oxygen coordination favorable for crystal formation. Larger-scale processes within the amorphous form can also have an important role. The evolution of TiO<sub>2</sub> nanostructures in ALD follows a path from amorphous layers to amorphous particles to metastable crystallites and ultimately to stable crystalline forms. The atomic scale processes of nucleation thus differ from the crystal-interface-dependent atomic processes of growth, and can be expected to have a different activation energy. The difference in the temperature dependences of nucleation and crystal growth can be exploited to find regimes favoring crystal growth and limiting nucleation.

## **Results and Discussion**

The nucleation and growth of crystalline STO from initially amorphous layers was investigated by sputter depositing amorphous STO thin films on room-temperature substrates and crystallizing via *ex situ* annealing. As described in the methods section, amorphous STO films were deposited by on-axis radio-frequency magnetron sputter deposition onto substrates held at room temperature, conditions that are expected to yield amorphous layers. <sup>14,18</sup> STO was deposited at a rate of 15 nm h<sup>-1</sup> to total thicknesses of approximately 60 nm. The precise thickness of each as-deposited film was measured using x-ray reflectivity (XRR). As-deposited STO layers on both STO and SiO<sub>2</sub>/Si substrates exhibited grazing incidence x-ray scattering patterns consistent with an amorphous thin film, as in Figures 2(a) and (b). The slight difference in the intensities of the scattering patterns in Figures 2(a) and (b) arises from the different x-ray incident angles, and thus illuminated volumes, for STO on STO (3.2°) and STO on SiO<sub>2</sub>/Si (1.4°). All annealing and crystallization experiments were conducted in air.

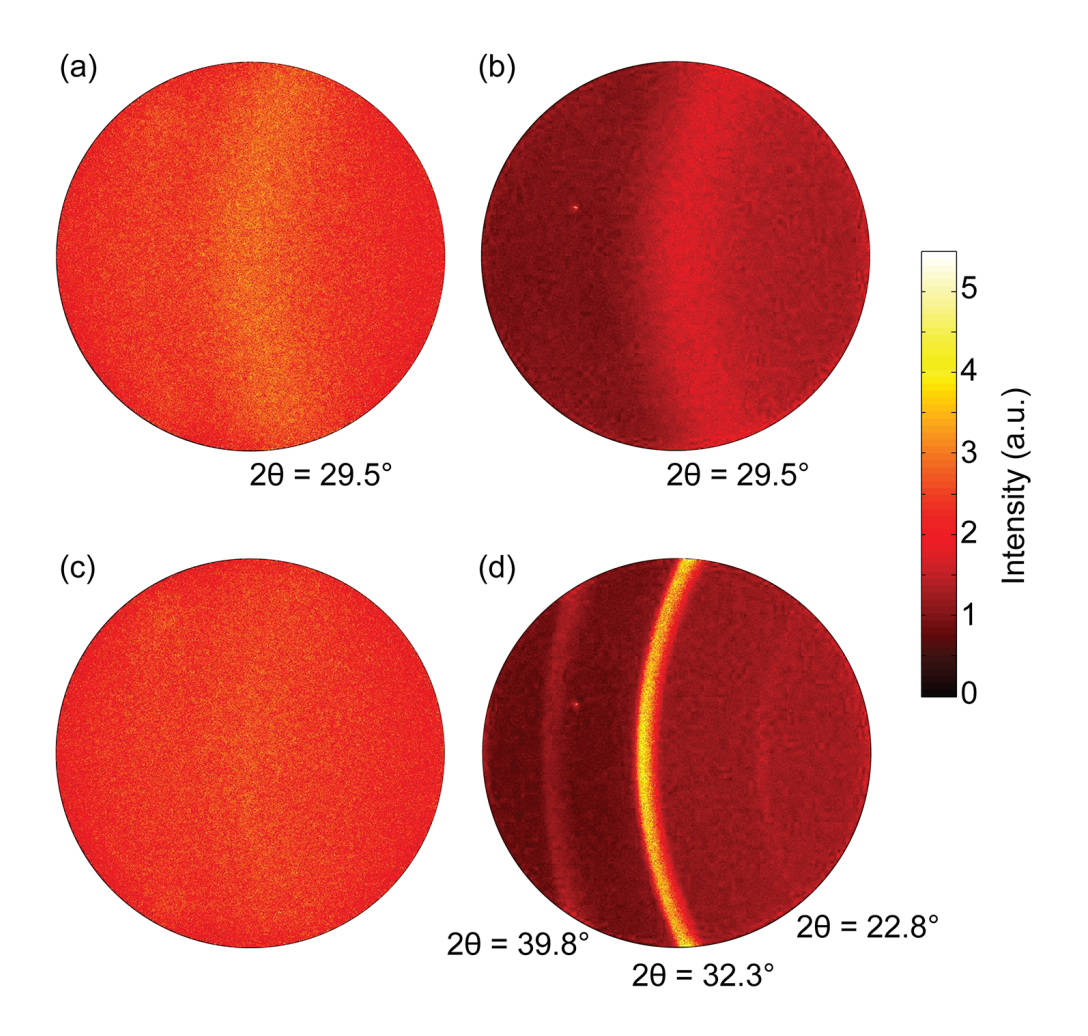


**Figure 2.** Grazing-incidence x-ray scattering patterns of (a) amorphous STO on (001) STO and (b) amorphous STO on SiO<sub>2</sub>/(001) Si, with a ring of scattering from amorphous STO at  $2\theta = 29.5^{\circ}$ . Scattering patterns of crystallized STO on (c) (001) STO and (d) SiO<sub>2</sub>/(001) Si. Rings of powder diffraction intensity appear  $2\theta$  angles of  $22.8^{\circ}$ ,  $32.3^{\circ}$ , and  $39.8^{\circ}$  arising from the (100), (110), and (111) reflections of polycrystalline STO appear following crystallization on SiO<sub>2</sub>/(001) Si.

The crystallization of STO on the STO (001) substrate results in the disappearance of the amorphous scattering signal without the appearance of polycrystalline diffraction rings. Figure 2(c) shows the x-ray scattering pattern of the same STO film shown in Figure 2(a) following

annealing at 650 °C for 5 min, a temperature and duration yielding full crystallization of the film. Transmission electron microscopy (TEM) provides further evidence of the crystallization of STO on STO by SPE. Annealing an as-deposited amorphous film at 600 °C for 32 min results in full crystallization, as shown by the cross-sectional high-resolution TEM images in Figure 3(a). The images were obtained from a <100>-oriented cross-sectional specimen and show lattice fringes with spacings that are consistent with <001> oriented STO. The preparation of the TEM samples is described in detail in the Methods section. The image with a larger field of view includes the sample surface, at which there is no interlayer between the amorphous carbon and the crystallized STO layer, indicating that the STO layer has fully crystallized under these conditions. The orientation of the lattice fringes is constant throughout the entire crystallized layer and identical to the substrate. These observations are consistent with the expectation that the layer is epitaxial and that the crystallization of STO on STO occurs via SPE.

For STO on SiO<sub>2</sub>/(001) Si, heating transforms the amorphous layer into a nanocrystalline microstructure. Figure 2(d) shows the x-ray scattering pattern of a crystallized STO thin film after annealing at 650 °C for 18 min, exhibiting a series of powder diffraction rings arising from (100), (110) and (111) reflections of STO. The integrated intensities of the (100) and (111) reflections are 3.3% and 19.8% of the intensity of the (110) peak, respectively. The peak positions and ratios of peak intensities agree with the powder x-ray diffraction pattern of STO,<sup>19</sup> indicating that the STO crystals form on SiO<sub>2</sub>/(001) Si in random orientations. The (100), (110) and (111) reflections have angular widths of 0.8°, 1.2°, and 1.5°, respectively, giving crystal sizes of 11 nm, 7 nm and 6 nm, respectively, based on Scherrer's formula. The x-ray reflections of STO thin films on SiO<sub>2</sub>/(001) Si crystallized at lower temperatures, from 450 °C to 600 °C, have similar angular widths and relative intensities. The 10 nm size of the STO crystals is much smaller than the total

film thickness of approximately 60 nm. The small STO crystal size, even after the completion of crystallization indicates that nucleation for STO on SiO<sub>2</sub>/(001) Si occurs within the volume of the film and is not limited to the free surface or to the STO/SiO<sub>2</sub> interface.

The crystallized STO layer and SiO<sub>2</sub>/(001) Si substrate are shown in the high-resolution TEM image in Figure 3(b) for a STO layer with an initial thickness of 61 nm heated to 600 °C for 36 min. The image was obtained from a Si <110>-oriented cross-sectional specimen. The spacing of the fringes is 2.76 Å, which matches the spacing of {110} planes in STO and is indicative of the local orientation of the crystallized STO. A high-resolution image of one STO nanocrystal within the layer exhibits lattice fringes with a misorientation of 11° with respect to the Si substrate. Other domains containing {110} crystal planes, with different angular orientations with respect to Si, were also observed in the high-resolution TEM analysis. Figure 3(b) shows a high-resolution TEM image in which a STO single lattice orientation is apparent across the entire image. The crystalline domain size in Figure 3(b) is on the order of tens of nanometers, which is larger than the mean value of the crystal size, determined from the widths of STO x-ray reflections. The difference between crystal sizes estimated with these methods can arise from inhomogeneity in the grain size of the polycrystalline STO.

Insight into the kinetic mechanism of crystallization can be obtained by examining the structure of partially crystallized STO layers. The evolution of the scattered x-ray intensity for an amorphous STO layer on (001) STO for a series of crystallization times at 600 °C is shown in Figure 4(a). The data shown in Figure 4(a) were acquired in a series of separate heating steps, each of which was followed by x-ray scattering characterization. The integrated intensity of the scattering feature arising from amorphous STO is shown as a function of heating time for annealing temperatures from 450 °C to 650 °C in Figure 4(b). The intensity of scattering arising from amorphous STO

decreases continuously with increasing annealing time. Details of the determination of the x-ray intensity scattered from amorphous STO are given in the Methods section. The intensity in the angular range of scattering from the amorphous layer is slightly higher than the background intensity even at long annealing times, an effect that is accounted for in the analysis below. We hypothesize that this difference, which is on the order of 10-30% of the total intensity of the scattering from the amorphous layer, may arise from small differences in the run-to-run alignment of the sample on the x-ray diffractometer, the formation of very small crystallites, or scattering from surface contamination accumulated during processing.

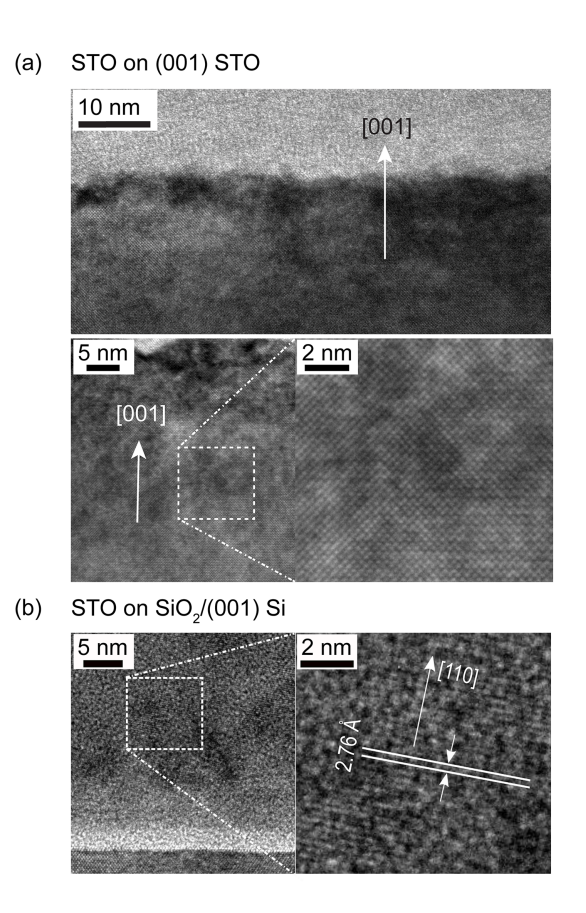


**Figure 3.** High-resolution TEM micrographs of fully crystallized STO films on (a) (001) STO and (b)  $SiO_2/(001)$  Si substrates.

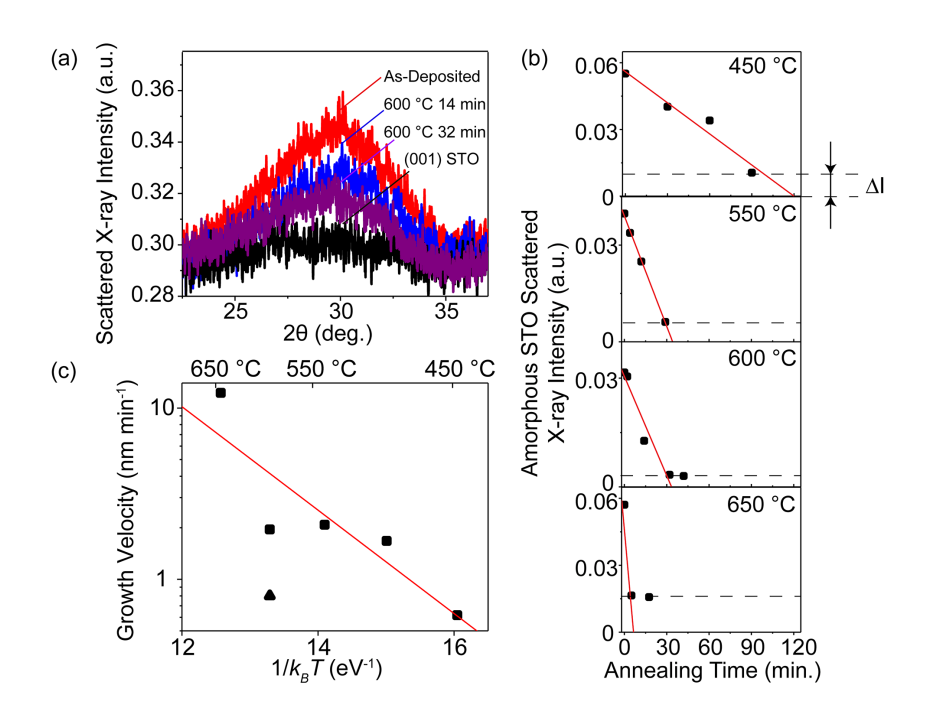


**Figure 4.** (a) Grazing-incidence x-ray scattering intensity for an STO film deposited on (001) STO and annealed at 600 °C in a series of steps with the indicated total duration. The curves represent as-deposited (red), partially crystallized (blue), and fully crystallized (purple) layers. Scattering intensity from the bare STO substrate (black) is shown for comparison. (b) Integrated x-ray intensity from the amorphous STO as a function of annealing time at temperatures of 450 °C, 550 °C, 600 °C, and 650 °C. The lines indicate the fit used to determine the crystalline/amorphous interface velocity at each temperature. (c) Growth velocities determined using the data shown in (b) (squares) and growth velocity at 600 °C determined using XRR (triangle). The line is a fit to determine the effective activation energy.

The growth velocity for crystallization of STO on (001) STO via SPE was determined using the rate of decrease of the scattered x-ray intensity from the amorphous layer. The x-ray intensity scattered from amorphous STO, I, can be modelled as  $I=C x(t) + \Delta I$ . Here C is a constant set by

the incident x-ray intensity, the scattering per unit volume from the amorphous layer, detector parameters, and beam footprint on the sample surface; x(t) is the thickness of the amorphous layer at time t, and  $\Delta I$  is the non-zero intensity of x-rays scattered from the fully crystallized film. The velocity v of the amorphous/crystalline interface is determined using  $v = \frac{dx}{dt} = \frac{1}{c} \frac{dI}{dt}$ . The constant C can be obtained by comparing the initial and final states,  $C = \frac{I_0 - \Delta I}{x_0}$ , where  $x_0$  is the initial thickness of the amorphous STO film and  $I_0$  is the initial scattered intensity of the as-deposited film. The growth velocity, v, is then:

$$v = \frac{dI}{dt} \frac{x_0}{I_0 - \Delta I} \tag{1}$$

The growth velocities found by applying equation (1) are plotted as a function of temperature in Figure 4(c). Velocities range from 0.6 nm min<sup>-1</sup> at 450 °C to 12.3 nm min<sup>-1</sup> at 650 °C. The velocity of 1.7 nm min<sup>-1</sup> at 500 °C has the same order of magnitude as the value of 3.7 nm min<sup>-1</sup> that can be inferred from the previously reported time required to crystallize a sputter-deposited STO film at the same temperature.<sup>14</sup> The differences between the rate reported here and the value from the literature are discussed in more detail below.

Previous studies of SPE of STO, as well as Si, SiGe, and other semiconductors have found that the growth velocity at temperature T can be described by an Arrhenius temperature dependence given by  $v(T) = v_0 e^{-E_a/k_B T}$ . <sup>12, 20-21</sup> Here  $E_a$  is the effective activation energy for the processes determining the velocity,  $v_0$  is a velocity prefactor, and  $k_B$  is the Boltzmann constant. A fit of this expression to the growth velocities reported in Figure 4(c) for the temperature range from 450 °C to 650 °C gives an activation energy of 0.7 eV.

The activation energy reported here is in reasonable agreement with the value of 0.77 eV observed for the crystallization of amorphous STO produced by ion implantation.<sup>12</sup> Other reported

activation energies range from 1.0 eV in an H<sub>2</sub>O atmosphere to approximately 2.1 eV in vacuum.<sup>13</sup> The activation energy of the amorphous/crystalline interface velocity for crystallization of STO on STO substrates depends on the gas ambient during annealing and the sample preparation method. Hydrogen, provided by the dissociation of water molecules at the surface, penetrates the amorphous layer to the amorphous-crystalline interface to increase the rate of the crystallization of amorphous STO. The crystallization velocity increases at higher concentration of diffusing hydrogen at the interface and exhibits a lower activation energy.<sup>13, 22</sup> The differences in activation energy and velocity reported here may thus arise from sensitivity to the ambient atmosphere during crystallization.

XRR studies provide further support for the crystallization of STO on (001) STO through the motion of a planar crystal/amorphous interface by SPE. Figure 5(a) shows XRR curves for an amorphous STO layer on a STO substrate for a series of annealing times at 600 °C. The XRR curve fit employed a two-layer model consisting of an amorphous STO layer on a uniform underpinning layer consisting of the STO substrate and crystallized STO layer. The densities of amorphous STO and crystalline STO were constrained in the range 4.2 ± 0.1 g cm<sup>-3</sup> and at 5.1 g cm<sup>-3</sup>, respectively, based on their literature values. <sup>13,23-24</sup> Thickness and roughness parameters for reflectivity curve fits are shown in Table 1. It is apparent from the XRR study that the amorphous layer thickness decreases continuously as a function of time during crystallization, as in Figure 5(b).

The XRR data indicates that a sample annealed at 600 °C for 35 min has a remaining amorphous layer with a thickness of approximately 10 nm. The TEM and XRD data, however, show that a separate sample nominally annealed at 600 °C for 32 min is already fully crystallized. This small difference can arise from uncertainty in the annealing temperature and time, including factors

associated with the loading of the samples within the furnace at each step. In addition, there is a slight shift between the XRR data and fit at low  $2\theta$  angles near the regime of total external reflection for the sample annealed at 600 °C for 35 min exhibits. Despite difficulties in fitting this regime, we note that the thickness measured using the fit is essentially given by the fringe spacing at higher  $2\theta$  angles, where the fit is a good match to the data.

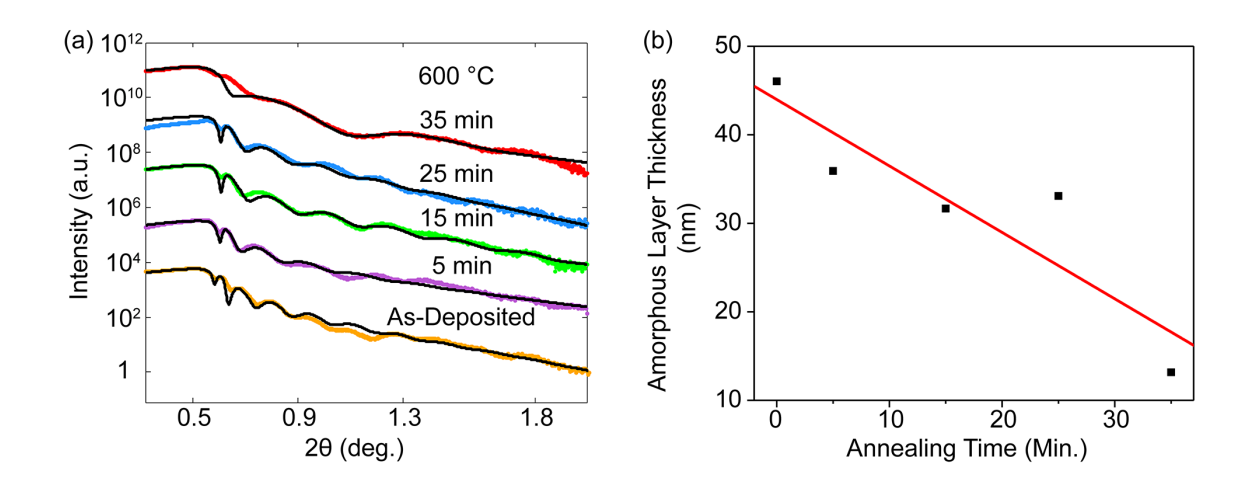


**Figure 5.** (a) XRR measurements of as-deposited amorphous STO on STO (orange) and after annealing at 600 °C for 5 min (purple), 15 min (green), 25 min (blue), and 35 min (red). Black lines show calculated reflectivity curves using the parameters given in the text. The intensity of the annealed samples has been shifted vertically to allow the curves to be distinguished. (b) Amorphous STO layer thickness, derived from the fringe spacing in XRR data, as a function of annealing time at 600 °C.

The velocity determined from the rate of amorphous/crystal interfaces motion in Figure 5(b) is 0.8 nm/min, which is slightly less than the value deduced from the x-ray scattering data (1.9 nm/min), but consistent with the overall temperature dependence of the crystallization velocity. The discrepancy in crystallization front velocities for these two samples can be explained by a

combination of random and systematic errors: temperature variation by several °C in the furnace can result in a velocity variation of 0.5 nm/min by applying the Arrhenius relationship, and the magnitude of  $\Delta I$ , as discussed earlier with respect to equation (1), can influence the velocity as much as 0.2 nm/min. The continuously decreasing thickness and the constant roughness of the STO interface are signs of crystallization at a planar crystalline/amorphous interface.

**Table 1.** Thickness and interface roughness determined from XRR measurements during the crystallization of amorphous STO on a crystalline STO substrate.

STO/STO annealing conditions	Amorphous STO layer thickness (nm)	Amorphous STO layer roughness (nm)	Substrate/crystallized STO interface roughness (nm)
As-deposited	46.04	1.06	2.38
600 °C 5 min	35.92	0.74	2.55
600 °C 15 min	31.67	1.07	1.72
600 °C 25 min	33.07	1.24	2.46
600 °C 35 min	13.17	0.66	2.20

The crystallization of STO on SiO<sub>2</sub>/(001) Si lacks the crystalline template provided by the STO substrate and instead occurs by a nucleation and growth process that results in a nanocrystalline microstructure. The time dependence of the intensity of x-ray scattering from amorphous STO layers on SiO<sub>2</sub>/(001) Si at an annealing temperature of 600 °C is shown in Figure 6(a). Intensity rings appear in the diffraction pattern after annealing for 16 min, indicating the formation of randomly oriented polycrystalline STO and marking the point when a large number of nuclei have formed at this temperature. The nucleation time depends on the temperature of the crystallization process.

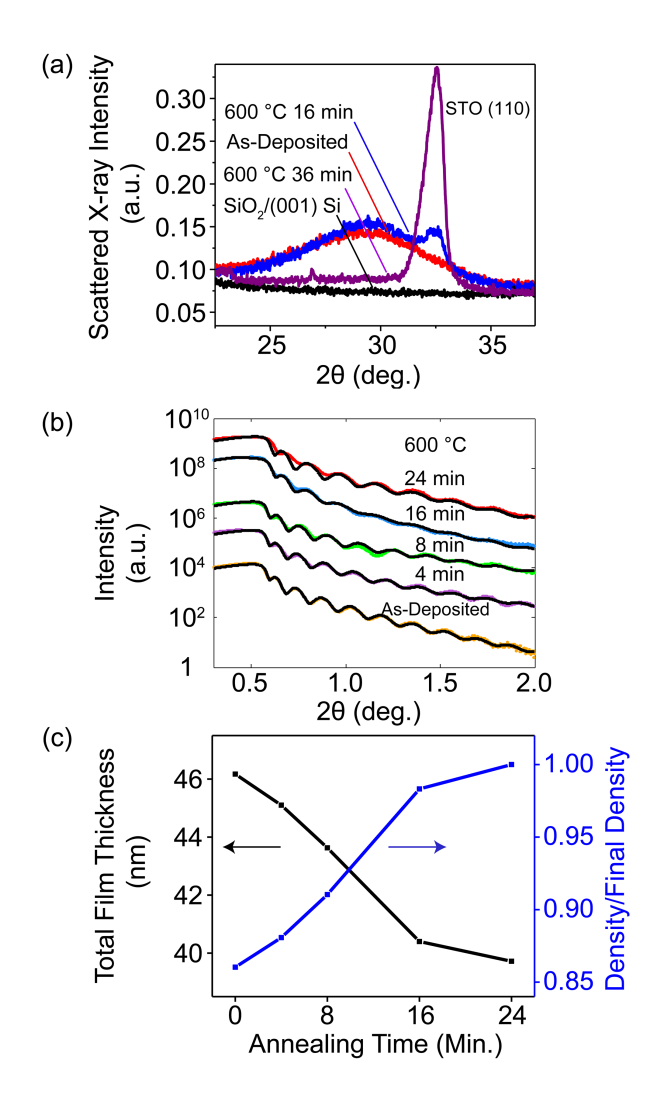


**Figure 6.** (a) Grazing-incidence x-ray scattering intensity for an STO layer deposited on SiO<sub>2</sub>/(001) Si substrate and annealed at 600 °C for different time periods. The curves represent asdeposited (red), partially crystallized (blue), and fully crystallized (purple) films. (b) XRR measurements of an as-deposited amorphous STO (orange), and the same sample annealed at 600 °C for 4 min (purple), 8 min (green), 16 min (blue), and 24 min (red). Fits using the parameters given in Table 2 are shown as black lines. (c) Film thickness and density as a function of annealing time at 600 °C.

XRR studies of crystallized STO on SiO<sub>2</sub>/(001) Si reveal the changes in the density of STO that

accompany crystallization. Figure 6(b) shows XRR curves of a STO layer deposited on  $SiO_2/(001)$  Si and annealed at 600 °C for different durations. The XRR fits for STO on  $SiO_2/(001)$  Si were performed with a three-layer model consisting of the STO film, native  $SiO_2$ , and Si substrate. The densities of the  $SiO_2$  and Si were set at 2.196 g cm<sup>-3</sup> and 2.329 g cm<sup>-3</sup>, respectively. The density of partially crystallized STO film was allowed to vary between the densities of amorphous and crystalline STO. The thickness and roughness derived from the fits are shown in Table 2. The XRR study shows that the STO thickness decreases upon crystallization, from 46 nm to 40 nm, as shown in Figure 6(c), indicating that the as-deposited density of amorphous STO is 87% of the density of crystalline STO. The observed change in density upon crystallization is consistent with reported densities of  $4.2 \pm 0.1$  g cm<sup>-3</sup> and 5.1 g cm<sup>-3</sup> for amorphous and crystalline STO, respectively.<sup>13, 23, 25</sup> The XRR results thus indicate that a volume contraction of on the order of 13% can be expected during the crystallization of amorphous STO thin films.

**Table 2.** Thickness and interfaces roughness determined from XRR measurements during the crystallization of amorphous STO on an  $SiO_2/(001)$  Si substrate.

STO/SiO <sub>2</sub> / (001) Si annealing conditions	Total thickness of polycrystalline and amorphous STO layers (nm)	STO roughness (nm)
As-Deposited	46.17	0.79
600 °C 4 min	45.10	0.13
600 °C 8 min	43.63	0.10
600 °C 16 min	40.40	0.74
600 °C 24 min	39.72	0.77

The role of nucleation in the crystallization of STO on  $SiO_2/Si$  can be quantified by considering the nucleation time  $t^*$ , which we define to be the longest time at which the x-ray intensity scattered from amorphous STO is equal to its as-deposited value. The  $t^*$  for STO on  $SiO_2$  is sufficiently long that at low temperatures it exceeds the total crystallization time of STO on STO substrates. At 450 °C, for example, as in Figure 7(a),  $t^*$  is more than 14 h whereas the crystallization of STO on STO (001) is completed within 1.5 h. The nucleation time at 650 °C is less than the minimum practical annealing time, and thus was not measured.

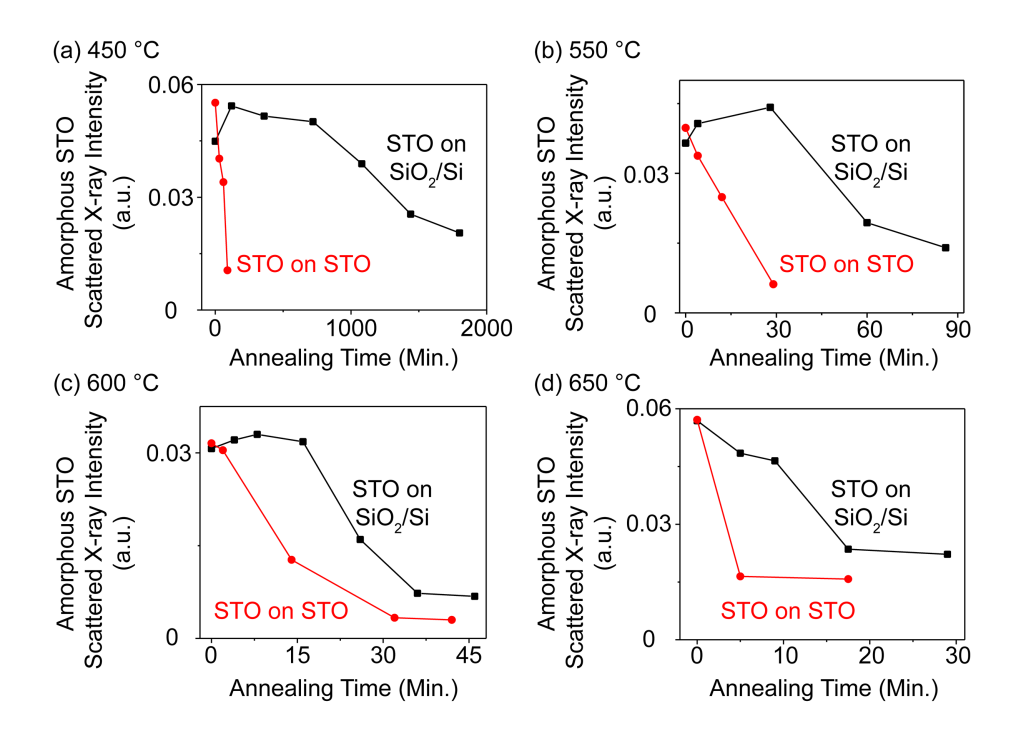


**Figure 7.** Time dependence of the x-ray intensity scattered from amorphous STO for STO on SiO<sub>2</sub>/(001) Si (black) and STO on (001) STO (red) for annealing temperatures of (a) 450, (b) 550, (c) 600, and (d) 650 °C.

In addition to the eventual decrease in the scattering from amorphous STO due to crystallization, there is also a reproducible increase in the scattered intensity from the amorphous layer of approximately 10% at short times in Figure 7, which we hypothesize arises from a rapid rearrangement of the amorphous structure at the initial stages of heating. There is also a slight narrowing of the angular distribution of intensity, as can be seen in the difference between the asdeposited and 16 min scattering patterns in Fig. 6(a). Annealing-induced changes in the amorphous scattering pattern in tin-doped indium oxide (ITO) amorphous thin films and linked to a unit-cell-scale rearrangement of the In-O bonding.<sup>3</sup> An evolution of the bonding configuration is also observed in photoelectron spectroscopy studies of annealed amorphous Al<sub>2</sub>O<sub>3</sub>.<sup>26</sup> Changes in electronic transport parameters are observed following heating of ITO films and are a further signature of structural rearrangement.<sup>27</sup> We note, however the rearrangement of the amorphous structure in ITO leads to large angular shifts of the amorphous scattering, which are not observed here. Amorphous STO incorporates multiple metal ions, and we hypothesize that an unknown local ionic rearrangement leads to the sharpening observed in Fig. 6(a) and the increase in amorphous scattering intensity observed at short times in Fig. 7.

Assuming that the nucleation process is also thermally activated, the nucleation time  $t^*$  for STO on SiO<sub>2</sub>/Si can be expressed using an Arrhenius temperature dependence:  $\frac{1}{t^*} = \frac{1}{t_0^*} e^{-E_b/k_BT}$ , as has previously been applied in the crystallization of glassy materials.<sup>24</sup> It is reasonable to expect a thermally activated nucleation time  $t^*$  because the time required to reach any given density of nuclei is inversely proportional to the nucleation rate.<sup>28</sup> Here  $1/t_0^*$  is a temperature-independent constant and  $E_b$  is the activation energy for nucleation. The variation of the experimentally observed  $t^*$  with temperature is shown in Figure 8(a). The nucleation activation energy obtained by fitting the expected temperature dependence to the experimentally observed nucleation time is 1.4 eV. The difference between the activation energies for crystal growth and nucleation is a key effect that allows us to find a window in which growth proceeds over long distances without

significant nucleation.

This relatively long nucleation time and high activation energy for nucleation of crystalline STO on SiO<sub>2</sub> provides the insight required to form STO and other complex oxides in sophisticated geometries. In such cases, crystalline STO can act as a crystalline template and materials with other compositions, such as SiO<sub>2</sub> can serve as a mask. As is apparent from the long nucleation time in Figure 7, SiO<sub>2</sub> can form interfaces with amorphous STO without providing nucleation sites for crystallization.

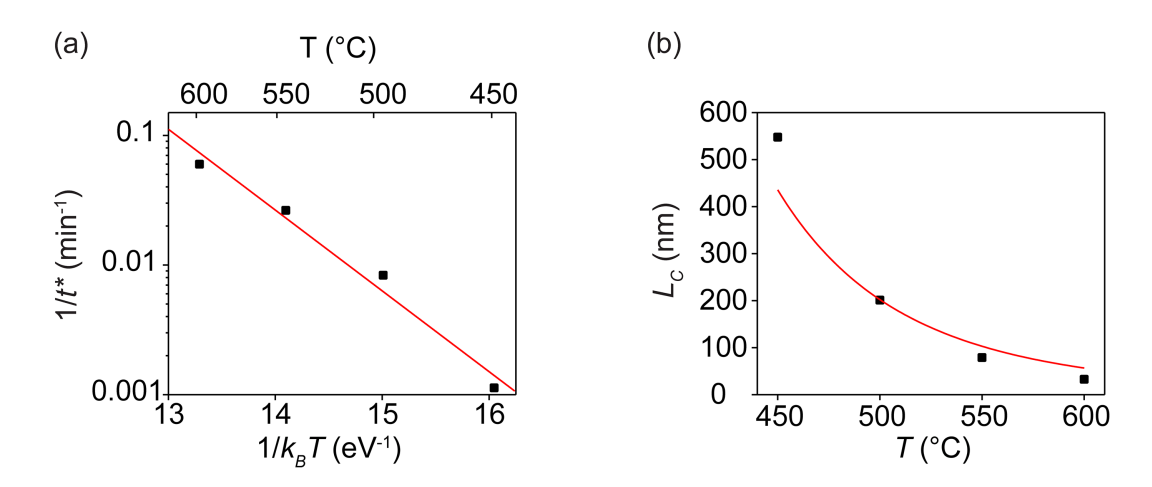


**Figure 8.** (a) Nucleation time for STO on  $SiO_2/(001)$  Si as a function of annealing temperature. The line is a fit to determine the effective activation energy. (b) Maximum STO crystallization distances before nucleation ( $L_C$ ) as a function of temperature. Points are the product of measured interface velocity and nucleation time, v and  $t^*$ . The temperature dependence predicted based on the measured activation energies of v and  $t^*$  is shown as a solid line.

The key parameter for the process of guiding the path of crystallization using a SiO<sub>2</sub> mask is the maximum film thickness or distance over which the amorphous STO can crystallize before the nucleation of crystalline STO occurs away from the moving interface. This maximum

crystallization distance,  $L_c$ , can be expressed as  $L_c = vt^*$ , where v is the velocity of the amorphous/crystalline interface due to SPE and  $t^*$  is the nucleation time. The values of  $L_c$  at annealing temperatures in the range of this study are plotted in Figure 8(b) based on values of v and  $t^*$  determined from STO on (001) STO and STO on SiO<sub>2</sub>/(001) Si, respectively. As would be expected from the difference in the activation energies of the two processes, the distance covered before nucleation increases as the temperature decreases. The largest  $L_c$  is in the present study is achieved at the relatively low temperature of 450 °C. Figure 8(b) indicates that for temperatures above 600 °C the crystallization lengths that can be achieved are less than 50 nm, lower than the thickness of as-deposited amorphous layers. Crystallizing amorphous films by SPE at temperatures above 600 °C can lead to highly defective crystalline layers due to nucleation away from the amorphous/crystalline interface. The high-temperature regime of Figure 8(b) is thus consistent with previous observations that STO solid-phase epitaxy becomes highly defective at high temperatures due to nucleation ahead of the crystallization interface. If v is a function of v and v which are both thermally activated, and can be expressed as:

$$L_C = vt^* = v_0 t_0^* e^{-(E_a - E_b)/k_B T} = v_0 t_0^* e^{-\Delta E/k_B T}$$
(2)

Figure 8(b) shows a plot of the measured product  $vt^*$ , illustrating that the maximum crystallization distance at different annealing temperatures can be estimated using equation (2).

The increase in the crystallization distance  $L_C$  at low temperatures, apparent in Figure 8(b), shows that flash heating or other rapid thermal processing techniques at high temperatures are not appropriate for suppressing nucleation to create thick single-crystalline layers of STO. A similar consideration is important in the crystallization of STO within high aspect ratio structures e.g. narrow and deep trenches or pores. Very large distances of the progression of crystalline interfaces are obtained at low temperatures e.g. 500 nm at 450 °C. Equation (2) further suggests that  $L_C$  can

be increased by optimizing the difference between the activation energies for nucleation and interface motion, for example by varying the environment during heating.

#### Conclusion

A comparison of the kinetics of crystallization of amorphous STO on STO single crystals and SiO<sub>2</sub>/Si substrates shows that at low temperatures SPE can result in the propagation of the crystalline/amorphous interface over large distances without leading to polycrystalline nucleation at non-epitaxial interfaces. The results indicate that it will be possible to synthesize singlecrystalline oxides in nanoscale geometries via crystallization from the amorphous layer. In addition to STO, crystallization by SPE has already been demonstrated in other complex oxides, for example in the perovskites EuTiO<sub>3</sub>, <sup>29</sup> CaTiO<sub>3</sub>, <sup>12</sup> BiFeO<sub>3</sub> on STO, <sup>30-31</sup> and SmNiO<sub>3</sub> on LaAlO<sub>3</sub>. <sup>32</sup> The discovery of the crystallization kinetics of STO thus points to methods for which a wide range of functional oxides, e.g. ferroelectrics and multiferroics, can be grown in complex geometries. There is now the exciting possibility that the difference between the kinetics of nucleation and amorphous/crystalline interface motion can be exploited in the crystallization of other complex oxide compositions and oxides in intricate geometries, including those relevant to electronic and thermal applications in which it has not been possible to integrate complex oxides. More generally, crystallization from an amorphous layer provides a route to the synthesis of nanoscale complexoxide materials that have been discovered and studied at the scale of individual structures, 33-34 but for which routes to large-scale fabrication for applications are lacking. In addition, there are indications in the literature that complex oxide electronic interfaces can be created by recrystallization.<sup>35</sup> The prospect of three-dimensional crystallization can also yield epitaxial interfaces, for example those hosting two-dimensional electron gases or functionality originating from control of the octahedral rotation.<sup>11, 28, 36-38</sup> Such interfaces have potentially widespread applications in three-dimensional nanoscale geometries, but can presently be synthesized only in planar epitaxial systems. Further exploration of nucleation and growth effects in these systems will facilitate the integration of complex oxides in 3D electronic, optoelectronic, and ionic devices.

#### Methods

STO substrates (Shinkosha Co., Ltd.) were purchased with one side polished. TiO<sub>2</sub> terminated-surfaces were prepared before growth by an annealing and deionized (DI) water treatment.<sup>39-40</sup> Substrate preparation employed a three-step process that consisted of annealing at 1000 °C for 1 h, sonicating the substrates in DI water to dissolve superficial strontium oxide that resulted from the first anneal, and annealing again at 1000 °C for 1 h. The STO substrates were then sonicated in acetone, isopropyl alcohol (IPA), methanol and DI water, for 2 min in each solvent. Unlike the STO substrates, the (001) Si substrates were not subjected to additional processing steps prior to solvent cleaning. This preserved the native SiO<sub>2</sub> layer on which amorphous STO was deposited.

Prior to depositing the amorphous STO films, the sputter-deposition vacuum chamber was evacuated to  $2 \times 10^{-6}$  Torr. STO layers were grown with the substrate at held room temperature at a total pressure of 18 mTorr with an Ar:O<sub>2</sub> flow-rate ratio of 6:1.

During the crystallization process, samples were inserted into a preheated furnace and reached temperatures 50 °C and 5 °C below the nominal temperature after less than 300 s and 600 s, respectively. The shortest reported time at 550, 650 and 600 °C is 300 s, thus there is some uncertainty in the reported temperature for these samples, which we have not explicitly considered in the analysis. The TEM cross-sectional specimens were prepared with a focused ion beam lift-out process. An electron-beam assisted carbon protective layer was deposited on the sample surface before its exposure to the Ga ion beam in order to prevent surface damage. High-resolution TEM imaging was conducted using a Tecnai TF-30 transmission electron microscope operated at 300 keV.

Grazing incidence x-ray diffraction studies employed a Bruker D8 Advance diffractometer with Cu Kα radiation at a wavelength of 1.54 Å, operating at a tube voltage 50 kV and current 1 mA.

The scattered intensity was recorded using a two-dimensional x-ray detector. The incident angle

of the x-ray beam was chosen, based on the beam width and sample size, to optimize the

amorphous peak signal by maximizing the x-ray footprint on the sample surface. The incident

angles for STO on STO and STO on SiO<sub>2</sub>/Si were 3.2° and 1.4° respectively. The 2θ angle at the

center of the detector was 30° for all measurements.

The crystallization kinetics of STO on STO and SiO<sub>2</sub>/Si substrates were compared by analyzing

the time evolution of the x-ray scattering intensity at a series of annealing temperatures. Integrating

the 2D detector images along the scattering ring azimuthal angle provide measurements of the

scattered intensity as a function of 20. The total x-ray intensity scattered from amorphous STO

was obtained by the following steps: (i) subtracting the scattering pattern of a bare substrate and

(ii) integrating the difference over the  $2\theta$  range from  $24^{\circ}$  to  $30^{\circ}$ . The upper limit of integration was

set at 30° to avoid the (110) STO peak at 32° in thin films deposited on  $SiO_2/(001)$  Si.

XRR data were collected using a Panalytical X'Pert MRD with monochromatic Cu Kα<sub>1</sub> x-ray

radiation at a wavelength of 1.5406 Å. XRR data shown in Figs. 5 and 6 were interpreted using

the interdiff model of the GenX software package.<sup>20</sup> A simpler interpretation of XRR results based

on a measurement of the mean period of the oscillation of the reflected intensity was used to

determine the initial thickness in growth rate results derived from x-ray scattering in Fig. 4.

**AUTHOR INFORMATION** 

**Corresponding Author** 

\*Email: \* (P.G.E) <u>pgevans@wisc.edu</u>

**Author Contributions** 

Yajin Chen and RB Jacobson constructed the sputtering system under the guidance of Paul G.

Evans and Max G. Lagally. Yajin Chen and M. Humed Yusuf were responsible for sample

25

synthesis and x-ray analysis with assistance from Yingxin Guan for the TEM analysis. Paul G. Evans, Thomas F. Kuech, Max G. Lagally, and Susan E. Babcock were responsible for the design and direction of the project and prepared the manuscript with Yajin Chen and M. Humed Yusuf.

# **Funding Sources**

This research was primarily supported by NSF Division of Materials Research through the University of Wisconsin Materials Research Science and Engineering Center (DMR-1121288 and DMR-1720415), including the work of YC, MHY, YG, SEB, TFK, and PGE. The work of RBJ and MGL, as described in the author contributions, was supported by the US Department of Energy Office of Basic Energy Sciences through grant no. DE-FG0203ER46028.

#### REFERENCES

- 1. Tighe, T. S.; Worlock, J. M.; Roukes, M. L. Direct Thermal Conductance Measurements on Suspended Monocrystalline Nanostructures. *Appl. Phys. Lett.* **1997**, *70*, 2687-2689.
- 2. Jang, J.; Moon, D.; Lee, H. J.; Lee, D.; Choi, D.; Bae, D.; Yuh, H.; Moon, Y.; Park, Y.; Yoon, E. Incorporation of Air-Cavity into Sapphire Substrate and its Effect on GaN Growth and Optical Properties. *J. Cryst. Growth* **2015**, *430*, 41-45.
- 3. Paine, D. C.; Whitson, T.; Janiac, D.; Beresford, R.; Ow-Yang, C. W.; Lewis, B. A Study of Low Temperature Crystallization of Amorphous Thin Film Indium-Tin-Oxide. *J. Appl. Phys.* **1999**, *85*, 8445-8450.
- 4. MacManus-Driscoll, J. L. Self-Assembled Heteroepitaxial Oxide Nanocomposite Thin Film Structures: Designing Interface-Induced Functionality in Electronic Materials. *Adv. Funct. Mater.* **2010**, *20*, 2035-2045.
- 5. Kim, D. H.; Sun, X.; Kim, T. C.; Eun, Y. J.; Lee, T.; Jeong, S. G.; Ross, C. A. Magnetic Phase Formation in Self-Assembled Epitaxial BiFeO<sub>3</sub>-MgO and BiFeO<sub>3</sub>-MgAl<sub>2</sub>O<sub>4</sub>

  Nanocomposite Films Grown by Combinatorial Pulsed Laser Deposition. *ACS Appl. Mater*. *Interfaces* **2016**, 8, 2673-2679.
- 6. Yan, L.; Yang, Y. D.; Wang, Z. G.; Xing, Z. P.; Li, J. F.; Viehland, D. Review of Magnetoelectric Perovskite-Spinel Self-Assembled Nano-Composite Thin films. *J. Mater. Sci.* **2009**, *44*, 5080-5094.
- 7. Taira, K.; Hirose, Y.; Nakao, S.; Yamada, N.; Kogure, T.; Shibata, T.; Sasaki, T.; Hasegawa, T. Lateral Solid-Phase Epitaxy of Oxide Thin Films on Glass Substrate Seeded with Oxide Nanosheets. *ACS Nano* **2014**, *8*, 6145-6150.

- 8. Ishiwara, H.; Yamamoto, H.; Furukawa, S.; Tamura, M.; Tokuyama, T. Lateral Solid-Phase Epitaxy of Amorphous Si Films on Si Substrates with SiO<sub>2</sub> Patterns. *Appl. Phys. Lett.* **1983**, *43*, 1028-1030.
- 9. Reinle-Schmitt, M. L.; Cancellieri, C.; Li, D.; Fontaine, D.; Medarde, M.; Pomjakushina, E.; Schneider, C. W.; Gariglio, S.; Ghosez, P.; Triscone, J. M.; Willmott, P. R. Tunable Conductivity Threshold at Polar Oxide Interfaces. *Nature Commun.* **2012**, *3*, 932.
- 10. Lee, D.; Lu, H.; Gu, Y.; Choi, S. Y.; Li, S. D.; Ryu, S.; Paudel, T. R.; Song, K.; Mikheev, E.; Lee, S.; Stemmer, S.; Tenne, D. A.; Oh, S. H.; Tsymbal, E. Y.; Wu, X.; Chen, L. Q.; Gruverman, A.; Eom, C. B. Emergence of Room-Temperature Ferroelectricity at Reduced Dimensions. *Science* **2015**, *349*, 1314-1317.
- 11. Ohtomo, A.; Hwang, H. Y. A High-Mobility Electron Gas at the LaAlO<sub>3</sub>/SrTiO<sub>3</sub> Heterointerface. *Nature* **2004**, *427*, 423-426.
- 12. White, C. W.; Boatner, L. A.; Sklad, P. S.; Mchargue, C. J.; Rankin, J.; Farlow, G. C.; Aziz, M. J. Ion-Implantation and Annealing of Crystalline Oxides and Ceramic Materials. *Nucl. Instrum. Methods Phys. Res.*, *Sect. B* **1988**, *32*, 11-22.
- 13. Simpson, T. W.; Mitchell, I. V.; Mccallum, J. C.; Boatner, L. A. Hydrogen Catalyzed Crystallization of Strontium Titanate. *J. Appl. Phys.* **1994**, *76*, 2711-2718.
- 14. Wang, F.; Badaye, M.; Yoshida, Y.; Morishita, T. Characterization of the Recovery and Recrystallization of SrTiO<sub>3</sub> Surface by Ion Channeling. *Nucl. Instrum. Methods Phys. Res., Sect. B* **1996**, *118*, 547-551.
- 15. Almeida, B. G.; Pietka, A.; Caldelas, P.; Mendes, J. A.; Ribeiro, J. L. Determination of Infrared Optical Parameters of SrTiO<sub>3</sub> Thin Films from the Reflectivity Spectrum. *Thin Solid Films* **2006**, *513*, 275-282.

- 16. Gutierrez, G.; Johansson, B. Molecular Dynamics Study of Structural Properties of Amorphous Al<sub>2</sub>O<sub>3</sub>. *Phys. Rev. B* **2002**, *65*, 104202.
- 17. Shi, J.; Li, Z. D.; Kvit, A.; Krylyuk, S.; Davydov, A. V.; Wang, X. D. Electron Microscopy Observation of TiO<sub>2</sub> Nanocrystal Evolution in High-Temperature Atomic Layer Deposition. *Nano Lett.* **2013**, *13*, 5727-5734.
- 18. Yadav, S.; Ghosh, S. Amorphous Strontium Titanate Film as Gate Dielectric for Higher Performance and Low Voltage Operation of Transparent and Flexible Organic Field Effect Transistor. *ACS Appl. Mater. Interfaces* **2016**, *8*, 10436-10442.
- 19. ICDD PDF Powder Diffraction File. *International Centre for Diffraction Data, Newtown Square, Pennsylvania, USA*.
- 20. Bjorck, M.; Andersson, G. GenX: an Extensible X-ray Reflectivity Refinement Program utilizing Differential Evolution. *J. Appl. Crystallogr.* **2007**, *40*, 1174-1178.
- 21. Aziz, M. J. The Mechanism of Solid-Phase Epitaxy. *NATO Adv. Sci. Inst. Ser.* **1992,** 222, 465-476.
- 22. Rankin, J.; McCallum, J. C.; Boatner, L. A. The Effect of Annealing Environments on the Epitaxial Recrystallization of Ion-Beam-Amorphized SrTiO<sub>3</sub>. *J. Mater. Res.* **1992**, *7*, 717-724.
- 23. Liu, J.; Shen, Z. J.; Nygren, M.; Su, B.; Button, T. W. Spark Plasma Sintering Behavior of Nano-sized (Ba, Sr)TiO<sub>3</sub> Powders: Determination of Sintering Parameters Yielding Nanostructured Ceramics. *J. Am. Ceram. Soc.* **2006**, *89*, 2689-2694.
- 24. Kempen, A. T. W.; Sommer, F.; Mittemeijer, E. J. Determination and Interpretation of Isothermal and Non-isothermal Transformation Kinetics; the Effective Activation Energies in Terms of Nucleation and Growth. *J. Mater. Sci.* **2002**, *37*, 1321-1332.

- 25. Cuffini, S. L.; Macagno, V. A.; Carbonio, R. E.; Melo, A.; Trollund, E.; Gautier, J. L. Crystallographic, Magnetic, and Electrical-Properties of SrTi<sub>1-x</sub>Ru<sub>x</sub>O<sub>3</sub> Perovskite Solid-Solutions. *J. Solid State Chem.* **1993**, *105*, 161-170.
- 26. Snijders, P. C.; Jeurgens, L. P. H.; Sloof, W. G. Structural Ordering of Ultra-thin, Amorphous Aluminum-Oxide Films. *Surf. Sci.* **2005**, *589*, 98-105.
- 27. Kim, M. G.; Kim, H. S.; Ha, Y. G.; He, J. Q.; Kanatzidis, M. G.; Facchetti, A.; Marks, T. J. High-Performance Solution-Processed Amorphous Zinc-Indium-Tin Oxide Thin-Film Transistors. *J. Am. Chem. Soc.* **2010**, *132*, 10352-10364.
- 28. Jiang, S. F.; ter Horst, J. H. Crystal Nucleation Rates from Probability Distributions of Induction Times. *Cryst. Growth Des.* **2011**, *11*, 256-261.
- 29. Shimamoto, K.; Hirose, Y.; Nakao, S.; Fukumura, T.; Hasegawa, T. Solid Phase Epitaxy of EuTiO<sub>3</sub> Thin films on SrTiO<sub>3</sub> (100) Substrates with Different Oxygen Contents. *J. Cryst*. *Growth* **2013**, *378*, 243-245.
- 30. Akbashev, A. R.; Plokhikh, A. V.; Barbash, D.; Lofland, S. E.; Spanier, J. E. Crystallization Engineering as a Route to Epitaxial Strain Control. *APL Mater.* **2015**, *3*, 106102.
- 31. Akbashev, A. R.; Chen, G. N.; Spanier, J. E. A Facile Route for Producing Single-Crystalline Epitaxial Perovskite Oxide Thin Films. *Nano Lett.* **2014**, *14*, 44-49.
- 32. Shi, J.; Zhou, Y.; Ramanathan, S. Colossal Resistance Switching and Band Gap Modulation in a Perovskite Nickelate by Electron Doping. *Nat. Commun.* **2014**, *5*, 4860.
- 33. Setter, N.; Damjanovic, D.; Eng, L.; Fox, G.; Gevorgian, S.; Hong, S.; Kingon, A.; Kohlstedt, H.; Park, N. Y.; Stephenson, G. B.; Stolitchnov, I.; Tagantsev, A. K.; Taylor, D. V.; Yamada, T.; Streiffer, S. Ferroelectric Thin films: Review of Materials, Properties, and Applications. *J. Appl. Phys.* **2006**, *100*, 051606.

- 34. Ramesh, R.; Spaldin, N. A. Multiferroics: Progress and Prospects in Thin Films. *Nat. Mater.* **2007**, *6*, 21-29.
- 35. Aurino, P. P.; Kalabukhov, A.; Tuzla, N.; Olsson, E.; Klein, A.; Erhart, P.; Boikov, Y. A.; Serenkov, I. T.; Sakharov, V. I.; Claeson, T.; Winkler, D. Reversible Metal-Insulator Transition of Ar-Irradiated LaAlO<sub>3</sub>/SrTiO<sub>3</sub> Interfaces. *Phys. Rev. B* **2015**, *92*, 155130.
- 36. Ide, K.; Nomura, K.; Hiramatsu, H.; Kamiya, T.; Hosono, H. Structural Relaxation in Amorphous Oxide Semiconductor, a-In-Ga-Zn-O. *J. Appl. Phys.* **2012**, *111*, 073513.
- 37. Cheng, G. L.; Tomczyk, M.; Lu, S. C.; Veazey, J. P.; Huang, M. C.; Irvin, P.; Ryu, S.; Lee, H.; Eom, C. B.; Hellberg, C. S.; Levy, J. Electron pairing without superconductivity. *Nature* **2015**, *521*, 196-199.
- 38. Rondinelli, J. M.; May, S. J.; Freeland, J. W. Control of octahedral connectivity in perovskite oxide heterostructures: An emerging route to multifunctional materials discovery.

  MRS Bulletin 2012, 37, 261-270.
- 39. Connell, J. G.; Isaac, B. J.; Ekanayake, G. B.; Strachan, D. R.; Seo, S. S. A. Preparation of Atomically Flat SrTiO<sub>3</sub> Surfaces Using a Deionized-water Leaching and Thermal Annealing Procedure. *Appl. Phys. Lett.* **2012**, *101*, 251607.
- 40. Boschker, J. E.; Tybell, T. Qualitative Determination of Surface Roughness by *in situ* Reflection High Energy Electron Diffraction. *Appl. Phys. Lett.* **2012**, *100*, 151604.

# Chen et al., Table of Contents Graphic

